



# Targeting inside charge carriers transfer of photocatalyst: Selective deposition of Ag<sub>2</sub>O on BiVO<sub>4</sub> with enhanced UV–vis–NIR photocatalytic oxidation activity

Tongyao Liu<sup>a,b</sup>, Xinqiang Zhang<sup>a,b</sup>, Fei Zhao<sup>a,b</sup>, Yuhua Wang<sup>a,b,\*</sup>

<sup>a</sup> Department of Materials Science, School of Physical Science and Technology, Lanzhou University, Lanzhou, 730000, China

<sup>b</sup> National and Local Joint Engineering Laboratory for Optical Conversion Materials and Technology, School of Physical Science and Technology, Lanzhou University, Lanzhou, 730000, China

## ARTICLE INFO

### Keywords:

Photocatalysis  
Selective heterostructure  
UV–vis–NIR light  
Charge density redistribution

## ABSTRACT

Rational regulation of photogenerated carrier separation and transfer is a significant strategy to optimize the photocatalytic activity. Given that the synergistic effect of crystal-face engineering and interfacial heterojunction modification, selective deposition of Ag<sub>2</sub>O nanoparticles onto BiVO<sub>4</sub> (040) facet has been realized successfully via the surfactant-assisted hydrothermal method combined with a facile coprecipitation process. As expected, compared to pure BiVO<sub>4</sub> and Ag<sub>2</sub>O, BiVO<sub>4</sub> (040)/Ag<sub>2</sub>O heterostructures have revealed great enhancements in photocatalytic O<sub>2</sub> evolution and methylene blue (MB) degradation capacities no matter under UV, Vis or NIR light irradiation. In-depth investigations confirm that the pronounced photooxidation performances are attributed to not only the outstanding capability in harvesting photon energies spanning from ultraviolet (UV) to near-infrared (NIR) regions, but also the accelerated charge carrier separation boosted by the charge density redistribution inside the BiVO<sub>4</sub> homojunction.

## 1. Introduction

In the situation of urgent renewable-energy and green-environment demands, photocatalytic water splitting and wastewater purification driven by sunlight have been attractive topics [1–3]. As a star material, monoclinic scheelite BiVO<sub>4</sub> is getting more attentions in photocatalytic oxidation reactions because of its sufficient photocatalytic response, high valance band (VB) potential and great stability [4,5]. Beyond that, obvious work function difference of (040) facet and (110) facet induces spatial charge separation and transfer inside BiVO<sub>4</sub>, thus results in the certain facet of BiVO<sub>4</sub> prefers reduction while another facet favors oxidation [6–8]. Even so, some inferior surface properties of BiVO<sub>4</sub> such as high surface-charge recombination rate and the weak surface adsorption capacity still restrict the utilization of charge carriers, thus hamper the full exploitation of its oxidizing capacity [9,10].

To overcome these above drawbacks of BiVO<sub>4</sub>, coupling crystal-face engineering with selective interfacial modification has been proven to be an effective strategy in the past decades [11–14]. Li. et al. have presented that loading of reduction co-catalyst (Ag, Au, Pt) on the electrons enriched (040) facet and deposition of oxidation co-catalyst (MnO<sub>x</sub>, PbO<sub>2</sub>, Co<sub>3</sub>O<sub>4</sub>) on the holes enriched (110) facet selectively

could expedite the charge separation, and further improve the photocatalytic oxidizing capacity of BiVO<sub>4</sub> dramatically [6,15,16]. Recent investigations on crystal-face engineering have verified that the photocatalytic activity of BiVO<sub>4</sub> is highly relying on the exposure of (040) facets, which have lower energy barrier and higher charge carrier mobility than (110) facets [17,18]. Based on this principle, constructing selective facet contact heterojunctions, such as g-C<sub>3</sub>N<sub>4</sub>/Ag/BiVO<sub>4</sub> (040), Ag@AgCl/BiVO<sub>4</sub> (040) and Ag<sub>3</sub>PO<sub>4</sub>/Ag/BiVO<sub>4</sub> (040), has also been demonstrated an efficient approach to suppress the charge carriers recombination and accelerate the accumulation of oxidizing holes in BiVO<sub>4</sub> [1,18,19]. That is, it is necessary to construct BiVO<sub>4</sub>-based heterostructures with suitable interfacial crystal faces and well-matched energy band alignments, which are crucial to promote the charge carrier transfer and give full play to its photooxidation reactivity ability [20,21].

In addition, the insufficient utilization of solar light, especially the NIR light (~50% of solar light), also restricts the practical application of BiVO<sub>4</sub> in photocatalytic oxidation process [22,23]. Some pioneering researches have been reported that serving up-conversion phosphors as intermedium to absorb NIR light and then transfer specific energy to BiVO<sub>4</sub> to induce photocatalytic reactions (e.g., CaF<sub>2</sub>:Yb@BiVO<sub>4</sub>, BiVO<sub>4</sub>/

\* Corresponding author at: Department of Materials Science, School of Physical Science and Technology, Lanzhou University, Lanzhou, 730000, China.

E-mail address: [wyyh@lzu.edu.cn](mailto:wyyh@lzu.edu.cn) (Y. Wang).

<https://doi.org/10.1016/j.apcatb.2019.03.062>

Received 13 December 2018; Received in revised form 5 March 2019; Accepted 23 March 2019

Available online 01 April 2019

0926-3373/© 2019 Elsevier B.V. All rights reserved.

$\text{CaF}_2\text{:Er}^{3+}, \text{Tm}^{3+}, \text{Yb}^{3+}$ ) [24,25]. Although these works show the feasibility of using NIR light for photocatalysis, the narrow absorption band of light at 980 nm and low energy conversion efficiency still hinder the sufficient utilization of solar light. Recently, silver oxide ( $\text{Ag}_2\text{O}$ ) with a low energy bandgap (1.3 eV) has received more attention in the practical photocatalytic application, due to its great capacity in absorbing NIR light without further process [26,27]. Besides, on the basis of its relative high VB edge (1.5 eV vs NHE), it is feasible to drive necessary oxidation reaction for the split of water or degradation of organic pollutant molecules [28]. A more recent study reveals a novel  $\text{Ag}_2\text{O}$  sensitized  $\text{TiO}_2$  photocatalyst, which can operate enhanced charge carriers separation capacity over a broad range of sun light wavelength from UV to NIR regions [29]. In addition, Niu et al. have suggested that the deposition of  $\text{Ag}_2\text{O}$  onto  $\text{Bi}_2\text{O}_2\text{CO}_3$  facilitates inside charge transfer effectively, as well as inhibits the self-decomposition of  $\text{Ag}_2\text{O}$ , which maintains good photocatalytic cycle performance [30]. As a consequence, the fabrication of  $\text{Ag}_2\text{O}$  with proper semiconductor could not only broaden the spectrum absorption region of the substrate, but also enhance the photocatalytic activity and stability via the flexible charge carrier transfer.

Based on the above discoveries, serial  $\text{BiVO}_4$  (040)/ $\text{Ag}_2\text{O}$  selective heterostructures with different  $\text{BiVO}_4$  to  $\text{Ag}_2\text{O}$  molar ratios have been performed successfully via the surfactant-assisted hydrothermal method combined with a facile coprecipitation process. It is found that the selective deposition of  $\text{Ag}_2\text{O}$  onto  $\text{BiVO}_4$  (040) facet not only extends the light absorption edge of  $\text{BiVO}_4$  substance to NIR light region, but also improves the photocatalytic  $\text{O}_2$  generation and MB degradation efficiencies greatly no matter what kind of light irradiated. Ultimately, based on the experimental results, detailed mechanisms toward the improved photocatalytic capacity of  $\text{BiVO}_4$  (040)/ $\text{Ag}_2\text{O}$  heterostructures are proposed.

## 2. Results and discussion

The morphology and the detailed structures of the as-prepared samples are detected by SEM and TEM, as depicted in Fig. 1. It can be observed from Fig. 1a that the pure  $\text{Ag}_2\text{O}$  powders show agglomerated status with a size of 400–800 nm, and the  $\text{BiVO}_4$  exhibits an ideal truncated bipyramid shape with highly exposed (040) facet (Fig. 1b).

Reportedly, the SDS can selectively adsorb on the (110) facet of  $\text{BiVO}_4$  and then cover the ions deposition sites [31]. In this case, most of  $\text{Ag}^+$  from the  $\text{AgNO}_3$  solution prefer to adsorb on the (040) facet of  $\text{BiVO}_4$  and realize the selective deposition of  $\text{Ag}_2\text{O}$  at last. Actually, as shown in Fig. 1c, it is clearly that most  $\text{Ag}_2\text{O}$  nanoparticles are deposited dispersedly on the  $\text{BiVO}_4$  (040) facets while their (110) facets exhibit smooth surfaces, which is in well accordance with the theoretical prediction. Moreover, the uniform distribution of Ag element (Fig. 1d) and the selective attachment of  $\text{Ag}_2\text{O}$  nanoparticles on the  $\text{BiVO}_4$  (040) facets observed from the top and side TEM images (Fig. 1e and f) further confirm the realization of  $\text{BiVO}_4$  (040)/ $\text{Ag}_2\text{O}$  selective heterostructures via the assistant of SDS. The HRTEM image (Fig. 1g) of the selected region in Fig. 1f shows the distance of 0.27 nm between the lattice spacing, which could be assigned to the (111) plane of  $\text{Ag}_2\text{O}$ . What's more, the identities of the different phase are directly confirmed by the EDX elemental line scanning across the  $\text{Ag}_2\text{O}$ - $\text{BiVO}_4$  (040) facet (Fig. 1h). It can be seen that Bi and V signals increase from the left side to right side constantly, while the Ag signal exhibits an obvious peak at the interface of two phases, which further confirms the dispersion of  $\text{Ag}_2\text{O}$  nanoparticles on the  $\text{BiVO}_4$  (040) facets. It is noteworthy that the distribution of Ag element overlaps the distribution of Bi and V at the inner edge of the  $\text{BiVO}_4$  crystal (shadow area in Fig. 1h), indicating the tight coupling between  $\text{BiVO}_4$  and  $\text{Ag}_2\text{O}$  particles. Under this circumstance, the intimate and efficient interfacial contact between these two phases will accelerate the mobility of inner photogenerated carriers greatly, and the formation of  $\text{BiVO}_4$  (040)/ $\text{Ag}_2\text{O}$  selective heterostructures is expected to reveal a great synergistic effect in photocatalytic reactions.

The crystalline structures and elemental chemical status of the as-prepared photocatalysts have been investigated by XRD, Raman and XPS. As shown in Fig. 2a, the reflection of pure  $\text{BiVO}_4$  matches well with the monoclinic scheelite  $\text{BiVO}_4$  phase (JCPDS 14-0688). After the incorporation of  $\text{Ag}_2\text{O}$  into  $\text{BiVO}_4$ , two small peaks ( $32.8^\circ$  and  $38.1^\circ$ ) indexed to the (111) and (200) crystal planes of  $\text{Ag}_2\text{O}$  (JCPDS 41-1104) appeared distinctly, forecasting the effective combination of  $\text{Ag}_2\text{O}$  with  $\text{BiVO}_4$ . No other new peaks could be examined in all the obtained samples, indicating the high-purity property of  $\text{BiVO}_4$  (040)/ $\text{Ag}_2\text{O}$  composites. Furthermore, the experimental molar ratio of  $\text{Ag}_2\text{O}$  to  $\text{BiVO}_4$  in BA3 composite are determined to be 3.3:10 by ICP-OES, which

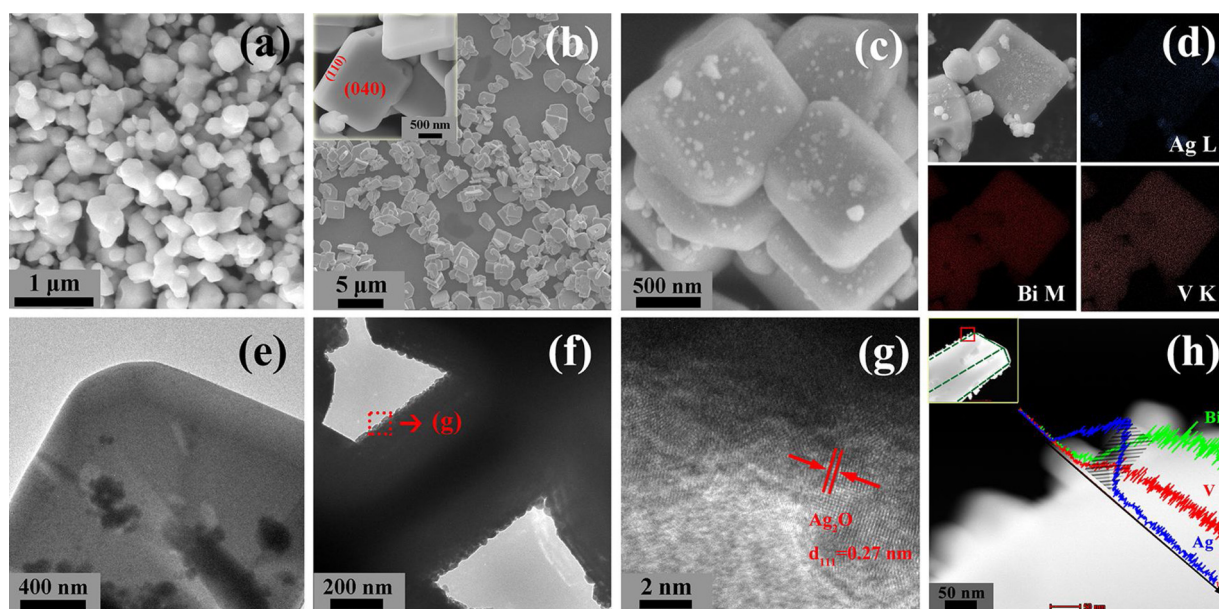


**Fig. 1.** SEM images of the obtained (a)  $\text{Ag}_2\text{O}$ , (b)  $\text{BiVO}_4$  (inset is the high-magnification SEM image) and (c) BA3 composite. (d) SEM mapping of Ag, Bi and V elements on the BA3 composite. TEM images of the BA3 composite from (e) top view and (f) side view, and (g) the HRTEM image of the selected region. (h) EDX elemental line scanning across the  $\text{Ag}_2\text{O}$ - $\text{BiVO}_4$  (040) facet and the inset shows the STEM image of the BA3 composite from side view.

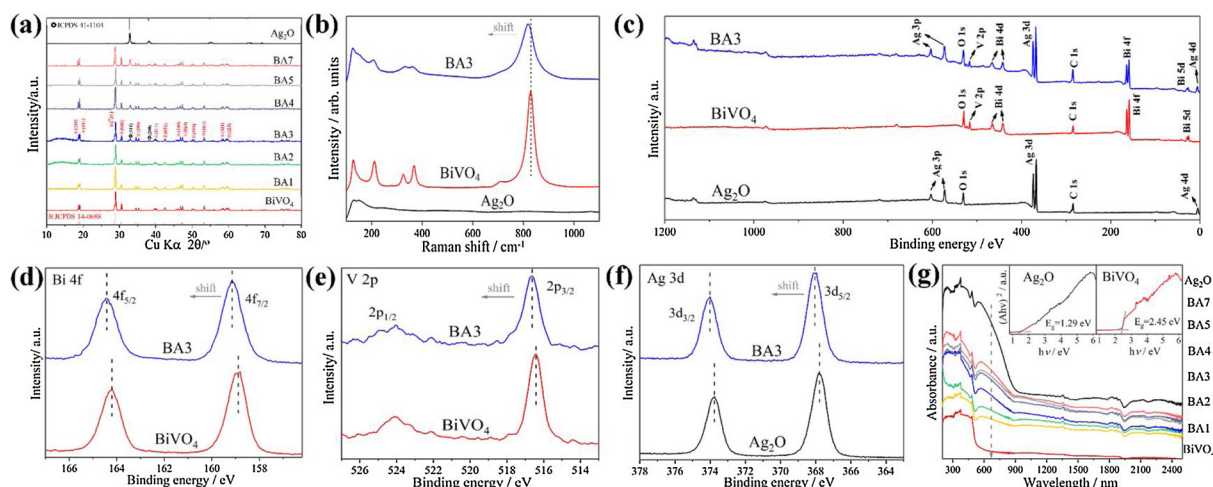


**Fig. 2.** (a) XRD patterns, (b) Raman spectra, (c) XPS survey spectra of the obtained  $\text{Ag}_2\text{O}$ ,  $\text{BiVO}_4$  and  $\text{BiVO}_4/\text{Ag}_2\text{O}$  composites. High-resolution XPS spectra of (d) Bi 4f, (e) V 2p for  $\text{BiVO}_4$ , BA3 composite and (f) Ag 3d for  $\text{Ag}_2\text{O}$ , BA3 composite. (g) UV-vis-NIR absorption spectra of the obtained  $\text{Ag}_2\text{O}$ ,  $\text{BiVO}_4$  and serial  $\text{BiVO}_4$  (040)/ $\text{Ag}_2\text{O}$  composites. The insets show the plots of  $(Ah\nu)^2$  versus photo energy for band gap energy ( $E_g$ ) of  $\text{Ag}_2\text{O}$  and  $\text{BiVO}_4$ .

suggests that the  $\text{Ag}_2\text{O}$  content is in good agreement with the expected theoretical values (3:10).

Raman spectroscopy is a powerful technique to characterize the bonding states and the local structure of composites. As displayed in Fig. 2b, the most intense vibrational band in pure  $\text{BiVO}_4$  is detected at around  $828.1\text{ cm}^{-1}$ , assigned to the symmetric V–O stretching mode [32]. Clearly, the introduction of  $\text{Ag}_2\text{O}$  particles gives rise to the shift of this Raman band into a lower frequency ( $817.3\text{ cm}^{-1}$ ). It is reported that the lower frequency of the Raman stretching band corresponds to the longer bond length [33], which means the V–O band in  $\text{BiVO}_4$  substrate has been elongated via the incorporation of  $\text{Ag}_2\text{O}$  and further demonstrates the effective interaction between  $\text{BiVO}_4$  and  $\text{Ag}_2\text{O}$ .

Moreover, the chemical states and elemental chemical compositions have also been analyzed by XPS. The survey XPS spectra (Fig. 2c) confirm the co-existence of Bi, V, O, Ag elements on the surface of BA3 composite and no other impurities are detectable, which agree well with the results of XRD analysis. The high-resolution XPS spectra of Bi 4p, V 2p and Ag 3d for different samples are displayed in Fig. 2d–f, respectively. The peak locations at 164.2, 158.9 and 524.0, 516.4 eV are closely corresponding to the  $\text{Bi}^{3+}$  and  $\text{V}^{5+}$  peaks in monoclinic  $\text{BiVO}_4$  [1,34]. Besides, the peaks at 373.8 and 367.8 eV in bare  $\text{Ag}_2\text{O}$  are assigned to  $\text{Ag } 3d_{3/2}$  and  $\text{Ag } 3d_{5/2}$  of  $\text{Ag}^+$  ions state totally [35]. It is noteworthy that all signals of Bi 4p, V 2p and Ag 3d in BA3 composite are slightly shifted to higher energy levels after combining  $\text{Ag}_2\text{O}$  with

$\text{BiVO}_4$ . This phenomenon could be attributed to the electron density change via the intense interaction effect between  $\text{BiVO}_4$  and  $\text{Ag}_2\text{O}$  in composites [36], and this result also implies the existence of hetero-junction interaction in the as-prepared  $\text{BiVO}_4$  (040)/ $\text{Ag}_2\text{O}$  hybrid photocatalysts, which will greatly expedite the operation of synergistic effect in these composites.

The light harvesting capacities of different samples are probed with the UV-vis-NIR absorption spectra and displayed in Fig. 2g. Clearly, pure  $\text{BiVO}_4$  shows a strong absorption ability in UV and Vis light regions and exhibits a steep absorption edge at  $\sim 510\text{ nm}$ , corresponding the bandgap energy of 2.45 eV. Furthermore, benefitted from the narrow bandgap energy of 1.29 eV, pure  $\text{Ag}_2\text{O}$  displays an obvious light absorption in the whole UV-vis-NIR range from 200 nm to 2500 nm. After the intimate coupling of  $\text{Ag}_2\text{O}$  and  $\text{BiVO}_4$ , all of  $\text{BiVO}_4$  (040)/ $\text{Ag}_2\text{O}$  composites exhibit intense absorption enhancement in UV and Vis light regions, and their absorption edges have successfully extended to NIR light region compared to pure  $\text{BiVO}_4$ . As a consequence, this heavy and broad light absorption of  $\text{BiVO}_4$  (040)/ $\text{Ag}_2\text{O}$  photocatalysts will not only enhance the UV and Vis light-excitation efficiency, but also generate great photocatalytic potential under the illumination of NIR light, which affords  $\text{BiVO}_4$  (040)/ $\text{Ag}_2\text{O}$  composites strong ability for harvesting full solar energy.

In order to prove the synergistic effect of  $\text{BiVO}_4$  (040)/ $\text{Ag}_2\text{O}$  composites on the photocatalytic capacity, the photodegradation of MB

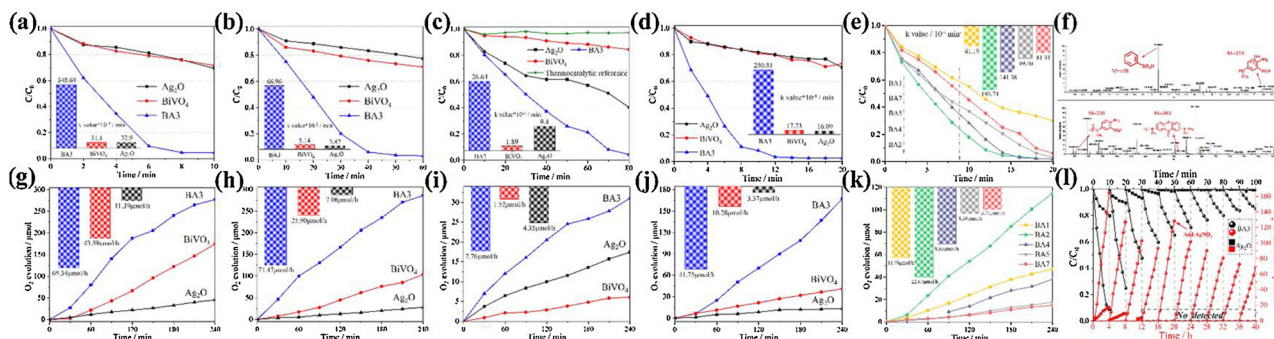


**Fig. 3.** Variation of MB solution concentration with irradiation time in the presence of pure  $\text{Ag}_2\text{O}$ ,  $\text{BiVO}_4$ , BA3 composite under (a) UV, (b) Vis, (c) NIR, (d) AM1.5 simulated solar light irradiation and (e) serial  $\text{BiVO}_4$  (040)/ $\text{Ag}_2\text{O}$  samples under AM1.5 simulated solar light irradiation (Inserts are the apparent rate constants of different samples). (f) Positive MS of the major production after photodegradation. Time courses of photocatalytic  $\text{O}_2$  generation over the pure  $\text{Ag}_2\text{O}$ ,  $\text{BiVO}_4$ , BA3 composite under (g) UV, (h) Vis, (i) NIR, (j) AM1.5 simulated solar light irradiation and (k) serial  $\text{BiVO}_4$  (040)/ $\text{Ag}_2\text{O}$  samples under AM1.5 simulated solar light irradiation (Inserts are  $\text{O}_2$  evolution rates of different samples). (l) Repeated AM1.5 simulated solar light-induced photocatalytic degradation of MB solution (black lines) and photocatalytic  $\text{O}_2$  generation (red lines) over pure  $\text{Ag}_2\text{O}$  (cubes) and BA3 composite (spheres).



solution and photocatalytic O<sub>2</sub> evolution are investigated as shown in Fig. 3. For comparison, the photocatalytic oxidizability of bare Ag<sub>2</sub>O and BiVO<sub>4</sub> are also tested under the same experimental conditions. Predictably, limited degradation degrees of MB solution are observed with the existence of bare Ag<sub>2</sub>O and BiVO<sub>4</sub> under the irradiation of either UV light (Fig. 3a) or Vis light (Fig. 3b), which are ascribed to the high recombination probability of the photo-induced carriers [18,37]. Interestingly, as indicated in Fig. 3c, the bare Ag<sub>2</sub>O is detected as possessing an obvious NIR light photocatalytic activity that about 60% of MB has been degraded within 80 min, while no degradation of MB solution is observed with the existence of BiVO<sub>4</sub>. This unique phenomenon could be attributed to the efficient NIR light absorption ability of Ag<sub>2</sub>O derived from its narrow band gap (1.29 eV). As expected, with selective deposition of Ag<sub>2</sub>O nanoparticles onto the (040) facet of BiVO<sub>4</sub>, the photocatalytic efficiencies of BA3 composite are remarkably improved no matter what kind of light irradiated, and the degradation rate constant of BA3 composite is above 15 times than that of bare BiVO<sub>4</sub> and Ag<sub>2</sub>O under the AM1.5 simulated solar light irradiation (Fig. 3d), farther confirming the crucial roles of optical absorption and charge separation in BiVO<sub>4</sub>-based heterostructures. In addition, the thermocatalytic reference experiment at 50 °C (MB suspension temperature during the NIR light irradiation) is carried out to verify whether the thermal energy dominates the photocatalytic degradation. As can be seen in Fig. 3c, the decolorization rate of MB at 50 °C with the exist of BA3 (green line) is negligible, demonstrating that the thermal energy generated by NIR irradiation is not high enough to induce the thermal degradation, and the degradation of MB under NIR light irradiation is attributed to the photocatalysis rather than temperature effect.

As for other BiVO<sub>4</sub> (040)/Ag<sub>2</sub>O composites (Fig. 3e), all of them exhibit higher solar light photocatalytic activities than pure BiVO<sub>4</sub> and Ag<sub>2</sub>O. The degradation rate reaches the maximum when the molar ratio of Ag<sub>2</sub>O-BiVO<sub>4</sub> increases to 3:10, and the further increase of the Ag<sub>2</sub>O content leads to the deterioration of photocatalytic activities. It is reasonable because the introduction of excess Ag<sub>2</sub>O onto BiVO<sub>4</sub> results in the blockade of incident light and the shielding of high-active (040) crystal face, thus inhibits the photocatalytic performances. The main intermediates of MB under AM1.5 simulated solar light irradiation are qualitatively determined via MS (Fig. 3f). Clearly, after 12 min solar light irradiation with the existence of BA3 composite, the peak belongs to the MB parent molecule ( $m/z = 284.2$ ) disappeared, along with several new peaks at  $m/z = 303$  (sulfoxide), 230 (2-amino-5-(N-methyl formamide) benzene sulfonic acid), 218 (2-amino-5-(methyl amino)-hydroxybenzene sulfonic acid) and 158 (benzenesulfonic acid) start to appear, suggesting the ring rupture and fragmentation of MB molecule structure during the irradiation. These results clarify that the degradation rather than adsorption should be the crucial mechanism in the photocatalytic reactions.

With the purpose of avoiding MB self-sensitization in the photocatalytic experiments, the degradation of colorless bisphenol A (BPA) and tetracycline (TC) under different light irradiation are carried out to assess the photocatalytic activity of the BA3 composite [38,39]. As shown in Fig. S1a, the pristine Ag<sub>2</sub>O and BiVO<sub>4</sub> exhibit limited photocatalytic performance that the degradation efficiencies are found to be 23.2% and 59.5% separately within 20 min of AM1.5 simulated solar light illumination. By contrast, the absorption peak at 277 nm of BPA decreased much more drastically that nearly 81.4% of BPA has been degraded over BA3 composite at the same light radiation time. Beyond that, the BA3 composite shows much stronger photocatalytic capacity in comparison to pristine Ag<sub>2</sub>O and BiVO<sub>4</sub> no matter under UV, visible or NIR light irradiation. Some intermediate products such as 4-Iso-propenylphenol ( $m/z = 134$ ) could be detected after photocatalytic process (Fig. S1b), suggesting the rupture and fragmentation of BPA molecule structure during the light irradiation [40,41]. Similarly, as displayed in Fig. S1c, BA3 composite also shows much more outstanding photocatalytic capacity in degradation of TC under various

light illumination compared with pure Ag<sub>2</sub>O and BiVO<sub>4</sub>, and the intermediate products exhibited in Fig. S1d further demonstrate the efficient decomposition of TC during the photocatalytic processes. Therefore, these photodegradation results of three model organic pollutants (MB, BPA and TC) all indicate that the BA3 composite is really an efficient UV-vis-NIR light-induced photocatalyst.

Besides, O<sub>2</sub> evolution has been measured for the photocatalytic water splitting process under different light irradiation to further demonstrate the enhanced photocatalytic oxidizability of BiVO<sub>4</sub> (040)/Ag<sub>2</sub>O composites. Obviously, the pure BiVO<sub>4</sub> exhibits high O<sub>2</sub> evolution rates under UV (Fig. 3g) and Vis light (Fig. 3h) irradiation but negligible O<sub>2</sub> evolution rate under NIR light (Fig. 3i) irradiation, which could be driven by the inner spatial separation of photogenerated charge carriers between (040) and (110) crystal faces and its broaden band gap (2.45 eV), respectively [7,8]. Fortunately, after the introduction of Ag<sub>2</sub>O, BA3 heterostructure shows further enhanced O<sub>2</sub> generation rates (69.34 μmol/h under UV light and 71.47 μmol/h under Vis light) in comparison to pure BiVO<sub>4</sub> (43.59 μmol/h under UV light and 25.90 μmol/h under Vis light). Beyond that, the NIR light-induced O<sub>2</sub> generation rate of BA3 heterostructure (7.76 μmol/h) is about 1.8 times and 5.1 times than that of bare Ag<sub>2</sub>O (4.35 μmol/h) and BiVO<sub>4</sub> (1.52 μmol/h) separately. These dramatical enhancements of the photocatalytic water splitting capacity forecast that Ag<sub>2</sub>O plays important roles in harvesting light and accelerating charge transfer in BiVO<sub>4</sub> (040)/Ag<sub>2</sub>O heterostructures. Benefited from these synergistic effects, serial BiVO<sub>4</sub> (040)/Ag<sub>2</sub>O composites include BA1, BA2 and BA3 show stepped-up O<sub>2</sub> generation activities under solar light irradiation (Fig. 3j, k). And the highest O<sub>2</sub> evolution rate of 41.75 μmol/h is reached at the Ag<sub>2</sub>O-BiVO<sub>4</sub> molar ratio of 3:10, which is significantly improved by more than 4 times compared to pure BiVO<sub>4</sub> (10.28 μmol/h) and Ag<sub>2</sub>O (3.37 μmol/h). Further increase of the Ag<sub>2</sub>O loading content (i.e. BA4, BA5 and BA7) leads to a decrease in O<sub>2</sub> evolution rate, corresponding to their photocatalytic MB degradation laws. Beyond that, the comparisons of photocatalytic degradation and O<sub>2</sub> generation performances among BA3 composite and other state-of-art BiVO<sub>4</sub>-based photocatalysts are displayed in Table S1. Obviously, the comparatively better photocatalytic performances are obtained under various light irradiation over the BA3 composite, demonstrating that the intimate contact between Ag<sub>2</sub>O and (040) facet of BiVO<sub>4</sub> not only expands the photo-sensitive range of BiVO<sub>4</sub> to NIR region, but also increases the utilization efficiency of UV and Vis photon energies in the photocatalytic oxidation process.

In addition to the photocatalytic activities, photo-stability are also significant in practical application. Therefore, repeated photocatalytic degradation of MB solution and photocatalytic O<sub>2</sub> generation are performed. As shown in Fig. 3l, the obvious activity inactivation is observed for pure Ag<sub>2</sub>O after the 3rd O<sub>2</sub> generation cycles and the 5th degradation cycles, which might be attributed to the strong photo-corrosion of the Ag<sub>2</sub>O particles [42,43]. After the deposition of Ag<sub>2</sub>O on to BiVO<sub>4</sub> (040) facet, a slighter deactivation in every O<sub>2</sub> generation and MB degradation cycling run and a higher photo-stability could be detected with the existence of BA3 composite. The high-resolution XPS spectra of Ag 3d for the used BA3 composite after cyclic reactions are detected as displayed in Fig. S2. Clearly, after 10 cyclic MB degradation (Fig. S2b) and O<sub>2</sub> generation (Fig. S2d) runs, except the intrinsic Ag<sup>+</sup> peaks of Ag<sub>2</sub>O appeared at 368.0 eV and 374.0 eV, two small peaks indexed to the reduced Ag<sup>0</sup> could be detected at 368.6 eV and 374.6 eV. This result reveals that the Ag<sub>2</sub>O are reduced to metallic Ag partly during the photocatalytic processes, which may be responsible for the descending MB degradation and O<sub>2</sub> generation activities after several cycles [29]. In addition, the mass of the BA3 sample after 10 cyclic MB degradation runs decreases to 28.31 mg, which only accounts for 56.6% of the initial BA3 sample mass (50 mg), hence the loss of photocatalyst during the cycling test is also an important factor in the decreased MB degradation activity. However, it is worth noting that even though the deactivation could be observed in every MB degradation or O<sub>2</sub>

generation cycling run with the existence of BA3 composite, the decay rate is gradually reduced as the cycle index increased. This phenomenon could be attributed to that once a certain amount of metallic Ag is formed on the surface of  $\text{Ag}_2\text{O}$ , the following photogenerated electrons tend to transfer to the  $\text{Ag}^0$  sites and are then captured by oxygen to form the  $\text{H}_2\text{O}_2$  ( $\text{O}_2 + 2\text{e}^- + 2\text{H}^+ = \text{H}_2\text{O}_2(\text{aq})$ ) or  $\text{H}_2\text{O}$  ( $\text{O}_2 + 4\text{e}^- + 4\text{H}^+ = 2\text{H}_2\text{O}(\text{aq})$ ) [44]. Therefore, after several cyclic MB degradation and  $\text{O}_2$  generation runs, the photocatalytic activities of BA3 composite tend to be stabilized gradually. These results all indicate that the efficient charge carrier separation and transfer between  $\text{Ag}_2\text{O}$  and  $\text{BiVO}_4$  accelerate the photo-stability of  $\text{BiVO}_4$  (040)/ $\text{Ag}_2\text{O}$  composites greatly. Beyond that, as shown in Fig. S3, in addition to the agglomeration of some particles on the surface of  $\text{BiVO}_4$  (040) facet, nearly no distinguishable morphology change is observed upon several runs of photocatalytic reactions, revealing the tight coupling between  $\text{Ag}_2\text{O}$  particles and  $\text{BiVO}_4$  (040) facet, and the great structural stability of BA3 composite.

Additionally, the wavelength-dependent  $\text{O}_2$  production AQY of BA3 has been studied and the results are displayed in Fig. S5 (detailed data of the measured  $\text{O}_2$  production rate and optical power density are listed in Table S2). The AQY decreases with increasing wavelength of the incident light, which corresponds to the optical absorption of the BA3 composite, clarifying that the  $\text{O}_2$  evolution is primarily driven by the photo-induced charge carriers inside  $\text{BiVO}_4$  (040)/ $\text{Ag}_2\text{O}$  heterostructures [45,46].

As is known, photocatalytic activity largely depends on the separation and transfer efficiency of the photo-induced charge carriers [47,48]. To further account for the positive effect of the deposition of  $\text{Ag}_2\text{O}$  on the enhanced photocatalytic oxidation ability, the electrochemical properties of the obtained samples have been investigated under the selective conditions. Fig. 4a–c display the photocurrent

densities of pure  $\text{Ag}_2\text{O}$ ,  $\text{BiVO}_4$  and BA3 composite under different light irradiation. Clearly, some promote generations of photocurrent with great reproducibilities can be discerned for all electrodes under intermittent light irradiations, and the photocurrent spectra of the electrodes are strongly affected by the modification of  $\text{Ag}_2\text{O}$  particles. The BA3 composite show much higher photocurrent intensities than pure  $\text{Ag}_2\text{O}$  and  $\text{BiVO}_4$  under various light irradiation, indicating the introduction of  $\text{Ag}_2\text{O}$  onto the  $\text{BiVO}_4$  (040) crystal face greatly improves the separation efficiency of photogenerated electron-hole pairs. Furthermore, the I–V curves of different samples in the absence and presence of illumination (Fig. S4) further confirm the much more outstanding photo-response properties of BA3 composite than that of pristine  $\text{Ag}_2\text{O}$  and  $\text{BiVO}_4$  from 0.5 V to 1.4 V no matter under UV, Vis or NIR light irradiation [49,50]. Meanwhile, EIS is employed to investigate the dynamics of interfacial charge transfer in different semiconductors. As shown in Fig. 4d, compared with pure  $\text{Ag}_2\text{O}$  or  $\text{BiVO}_4$ , the BA3 composite exhibit smallest arc radius no matter the existence of AM1.5 simulated solar light illumination, suggesting that the BA3 heterostructure has the lowest charge transfer resistance and holds the strongest capacity in migrating photogenerated charge carriers, which are highly conducive for the improvement of its photocatalytic oxidation efficiency.

In order to clarify the main active oxidative species in the photocatalytic process and detect the transfer pathway of the photo-induced charge carriers, the trapping experiments of holes ( $\text{h}^+$ ),  $\cdot\text{OH}$  and  $\cdot\text{O}_2^-$  radicals are carried out under UV or Vis light illumination with the existence of  $\text{Na}_2\text{C}_2\text{O}_4$ , t-BuOH and purging  $\text{N}_2$  separately (Fig. 5a). It should be noted that  $\text{N}_2$  as the  $\cdot\text{O}_2^-$  scavenger has nearly no effect on the degradation efficiency of MB, while the addition of  $\text{Na}_2\text{C}_2\text{O}_4$  and t-BuOH results in the fast deactivation of BA3 composite for the photocatalytic oxidation of MB solution. These phenomena suggest that both

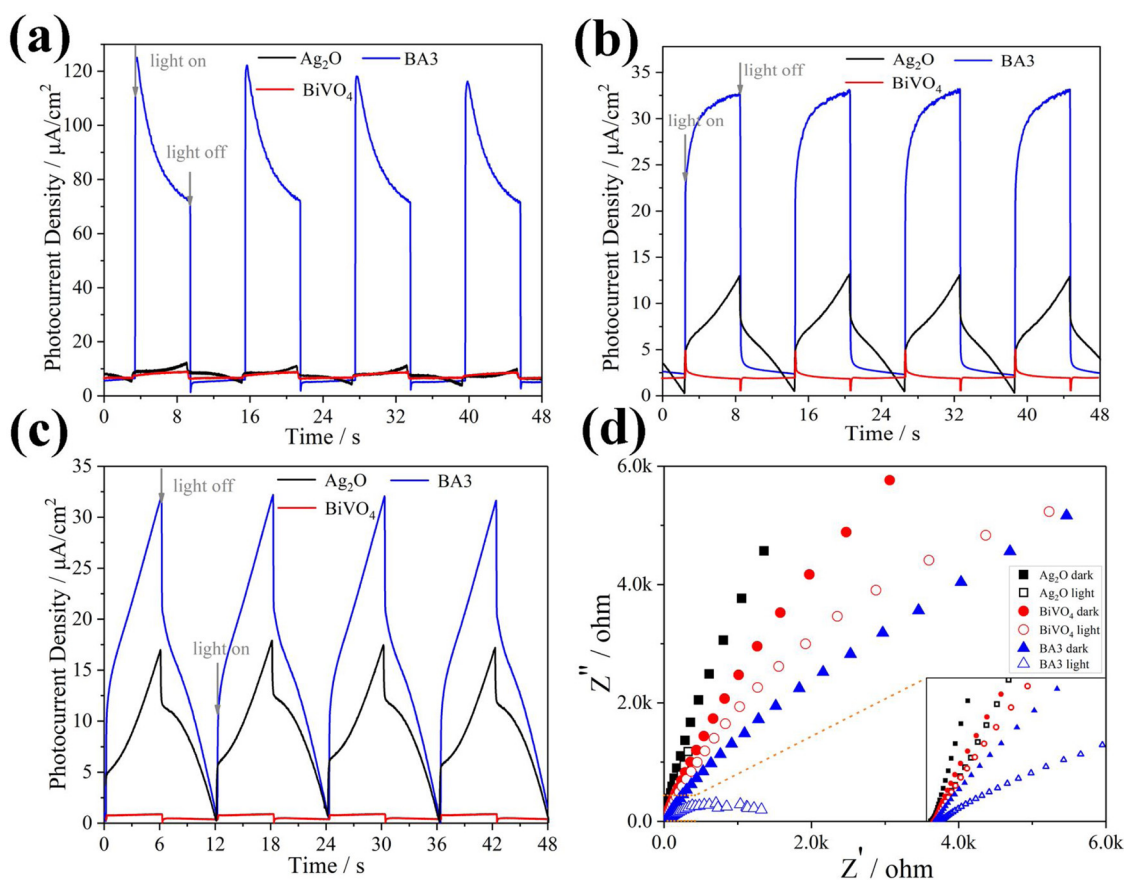


**Fig. 4.** Photocurrent density vs time (I–t) curves of pure  $\text{Ag}_2\text{O}$ ,  $\text{BiVO}_4$  and BA3 composite under (a) UV, (b) Vis and (c) NIR light irradiation. (d) EIS Nyquist plots of different samples in dark and under AM1.5 simulated solar light illumination (the inset shows the detail of the selected area).

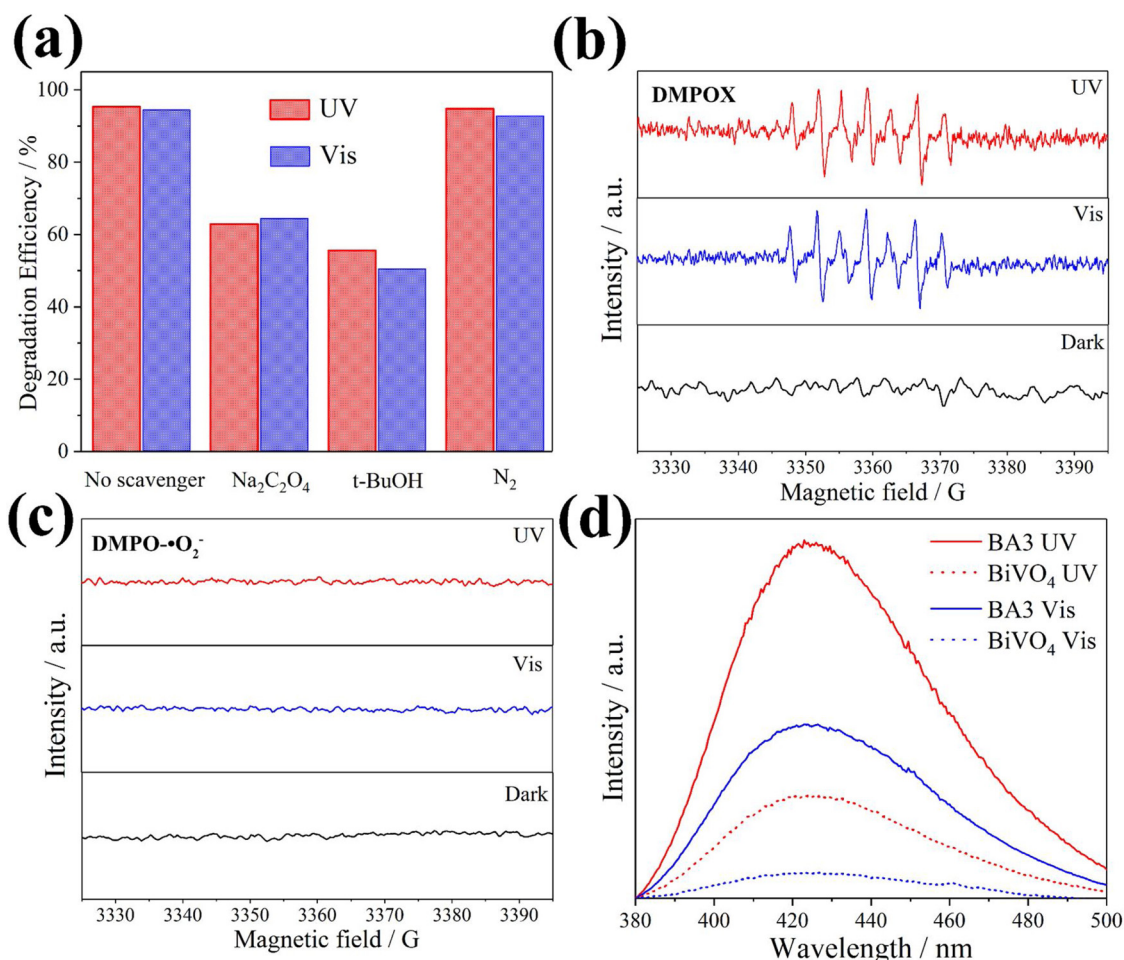


**Fig. 5.** (a) Degradation efficiency of MB solution by using different radical scavengers for BA3 composite after UV (10 min) or Vis (40 min) light illumination. DMPO spin-trapping ESR spectra of BA3 composite in (b) aqueous dispersion and (c) methanol dispersion under UV or Vis light irradiation. (d) Fluorescence spectra observed in BA3 or pure BiVO<sub>4</sub> dispersed TA solution after UV or Vis light irradiation for 10 min:  $\lambda_{\text{ex}} = 315 \text{ nm}$ .

$\text{h}^+$  and  $\cdot\text{OH}$  radicals are the main reactive species and no  $\cdot\text{O}_2^-$  radicals involved in these photocatalytic oxidation processes. The involvement of  $\cdot\text{OH}$  and  $\cdot\text{O}_2^-$  are also verified by the ESR test directly. As shown in Fig. 5b, incubating BA3 composite with DMPO in H<sub>2</sub>O shows a rapid production of ESR spectra with seven characteristic peaks under UV and Vis light irradiation. This type of peaks can be assigned to a derivative of DMPO, 5,5-dimethyl-2-ketopyrrolidino-1-oxyl (DMPOX), resulting from the oxidation of DMPO by two  $\cdot\text{OH}$  radicals [51]. That is to say, the BA3 composite will generate plenty of  $\cdot\text{OH}$  radicals no matter under UV or Vis light irradiation [52,53]. On the contrary, no  $\cdot\text{O}_2^-$  signals can be detected from BA3 with or without light irradiation (Fig. 5c), which are consistent with the radicals trapping experiments displayed in Fig. 5a. To further detect the generation of  $\cdot\text{OH}$  radicals in different conditions directly, photoluminescence method is carried out with TA as the probe (Fig. 5d). As expected, compared with the BiVO<sub>4</sub> dispersed TA solution (dash lines), the BA3 dispersed TA solution (full lines) exhibit dramatically enhanced fluorescence intensities no matter under UV or Vis light irradiation. This result not only reflect more  $\cdot\text{OH}$  radicals generated with the exist of BiVO<sub>4</sub> (040)/Ag<sub>2</sub>O composites, but also confirm the efficient photogenerated  $\text{e}^-$ - $\text{h}^+$  separation in the BiVO<sub>4</sub> (040)/Ag<sub>2</sub>O heterostructures, which are beneficial for the photocatalytic degradation and water splitting.

The energy level alignment of a heterostructure is the predominant factor that it determines the interfacial dynamic behavior of photo-induced charge carriers across the heterointerface [21]. We proposed the energy level diagram of heterostructure through the following three steps. Firstly, UPS spectra of BiVO<sub>4</sub> and Ag<sub>2</sub>O (Fig. S6) are employed to

ascertain their respective ionization potentials (equal to the maximum of the valence band energies,  $E_{\text{VB}}$ ) [54]. According to previous reports,  $E_{\text{VB}}$  could be calculated by subtracting the width of the He I UPS spectra (Fig. S6) from the excitation energy (21.22 eV) [55–57], which are calculated to be 2.91 eV vs NHE (21.22–(18.34–4.47) = 7.35 eV vs  $E_{\text{vac}}$ ) and 1.67 eV vs NHE (21.22–(18.62–3.51) = 6.11 eV vs  $E_{\text{vac}}$ ) for BiVO<sub>4</sub> and Ag<sub>2</sub>O separately [57,58], implying the top of the VB of BiVO<sub>4</sub> (110) facet is 2.91 eV vs NHE [21]. Secondly, the CB energies ( $E_{\text{CB}}$ ) of BiVO<sub>4</sub> (110) facet and Ag<sub>2</sub>O are thus estimated at 0.46 eV vs NHE (2.91 eV–2.45 eV) and 0.38 eV vs NHE (1.67 eV–1.29 eV), respectively, from  $E_{\text{VB}} - E_{\text{g}}$ . Thirdly, combined with the reported VB and CB offset between (040) facet and (110) facet (0.37 eV and 0.42 eV separately), the  $E_{\text{VB}}$  and  $E_{\text{CB}}$  of BiVO<sub>4</sub> (040) facet could be calculated by 3.28 eV vs NHE (2.91 eV + 0.37 eV) and 0.88 eV vs NHE (0.46 eV + 0.42 eV), respectively. Therefore, the energy level diagram of the BiVO<sub>4</sub> (040)/Ag<sub>2</sub>O heterostructure has been obtained and illustrated Fig. S7.

According to the above experimental and theoretical results, schematic diagrams of the charge carrier separation and transport processes at the interface of BiVO<sub>4</sub> (040)/Ag<sub>2</sub>O composites are proposed in Fig. 6. As shown in Fig. 6A–a and -b, under NIR light illumination, only Ag<sub>2</sub>O can serve as a sensitizer because of its narrow band gap (1.29 eV). Driven by the electric potential difference between Ag<sub>2</sub>O and BiVO<sub>4</sub> (040) facet, the photo-induced electrons in the CB of Ag<sub>2</sub>O will migrate towards the CB of BiVO<sub>4</sub> (040) facet, while the primordial holes accumulated in the VB of Ag<sub>2</sub>O will expedite the oxidation of water into O<sub>2</sub> and the decomposition of organic pollutants into non-toxic substance



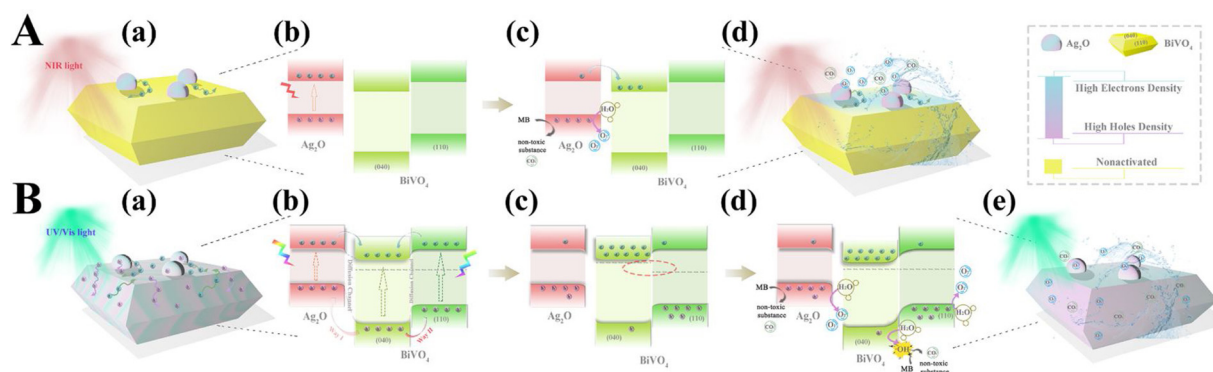


**Fig. 6.** Schematic diagram of the charge carrier separation and transport processes in BiVO<sub>4</sub> (040)/Ag<sub>2</sub>O composites under (A) NIR light and (B) UV or Vis light irradiation.

directly (Fig. 6A–c and -d). In this situation, the efficient separation of photogenerated electron-hole pairs boosts the generation of long-lived active holes in Ag<sub>2</sub>O, and then improves the NIR light-induced photocatalytic oxidation capacity dramatically.

On the other side, when BiVO<sub>4</sub> (040)/Ag<sub>2</sub>O composites are irradiated by UV or Vis light, both BiVO<sub>4</sub> and Ag<sub>2</sub>O could be excited to generate electrons and holes (Fig. 6B–a). Driven by the work function differences among BiVO<sub>4</sub> (040) facet (4.24 eV), BiVO<sub>4</sub> (110) facet (5.51 eV) and Ag<sub>2</sub>O (4.8–5.1 eV) [59,60], the electrons will flow from BiVO<sub>4</sub> (040) facet to Ag<sub>2</sub>O and BiVO<sub>4</sub> (110) facet together until their Fermi levels are aligned at the same electric potential (Fig. 6B–b) [61]. In this charge migration process, the depletion layers are generated and the bands are bent upward near the surface of (040) facet, while the accumulation layers are set up and the bands are bent downward near the surfaces of (110) facet and Ag<sub>2</sub>O. As a consequence, charge carrier diffusion channels have formed at the Ag<sub>2</sub>O–BiVO<sub>4</sub> (040) facet–BiVO<sub>4</sub> (110) facet interfaces.

In general, photoexcited electrons inside Ag<sub>2</sub>O and BiVO<sub>4</sub> (110) facet are likely transferred to the CB of BiVO<sub>4</sub> (040) facet simultaneously, while the holes accumulated in the VB of BiVO<sub>4</sub> (040) facet will migrate to that of Ag<sub>2</sub>O (Way I in Fig. 6B–b) and BiVO<sub>4</sub> (110) facet (Way II in Fig. 6B–b) theoretically, which follows the traditional “type-II heterojunction” charge transfer pathway [62]. Notably, the low VB potential of Ag<sub>2</sub>O (1.67 eV vs NHE) restricts the oxidation process of OH<sup>−</sup>/H<sub>2</sub>O to •OH (2.4 eV vs NHE) [35]. In this case, no matter under UV or Vis light irradiation, the BiVO<sub>4</sub> (040)/Ag<sub>2</sub>O composites dispersed TA solution should generate less •OH radicals and show lower fluorescence intensities compared with bare BiVO<sub>4</sub> dispersed TA solution [63,64]. However, the •OH trapping experiments (Fig. 5d) showed inconsistent result that much more •OH radicals generated in the presence of BiVO<sub>4</sub> (040)/Ag<sub>2</sub>O composites. Accordingly, the traditional “type-II heterojunction” charge transfer pathway is noneffective in BiVO<sub>4</sub> (040)/Ag<sub>2</sub>O composites, and most of the photo-induced holes migrate inside the BiVO<sub>4</sub> homojunction from the VB of BiVO<sub>4</sub> (040) facet to that of BiVO<sub>4</sub> (110) facet followed “Way II”, rather than along the interface between BiVO<sub>4</sub> (040) facet and Ag<sub>2</sub>O (Way I).

Under the above circumstance, presumably, charge density redistribution caused by the unbalanced charge carrier transfer will alter the relative Fermi levels position between (040) facet and (110) facet inside the BiVO<sub>4</sub> homojunction [1,18,61,65], as displayed in Fig. 6B–c. In this situation, free electrons pumped in BiVO<sub>4</sub> (040) facet will further flow to BiVO<sub>4</sub> (110) facet until their Fermi levels are aligned at the same level again, thus promotes the degree of interfacial band bending (Fig. 6B–d and e). Hereon, Mott–Schottky plots of BA3 composite are employed in dark and light conditions to verify the Fermi level shift inside BiVO<sub>4</sub>. As exhibited in Fig. S8, the Mott–Schottky curve in light shows lower slope than that in dark, which indicates the higher donor (electrons in n-type BiVO<sub>4</sub>) densities inside BiVO<sub>4</sub> with light irradiation [66], demonstrating the accumulation of electrons in the BiVO<sub>4</sub>.

Besides, it is found that the flat-band potential (which is determined by taking the x-intercept of a linear fit to the Mott–Schottky plots) of BA3 composite in light is distinctly lower than that in dark, suggesting that the accumulated electrons and unbalanced charge carrier transfer inside BiVO<sub>4</sub> further give rise to the up-shift of Fermi level under AM1.5 simulated solar light irradiation [67]. As a consequence, the driving force for charge carriers transfer has been accelerated rapidly inside BiVO<sub>4</sub> homojunction, thus promotes the photocatalytic activities ultimately.

In order to further prove the decisive effect of the charge density redistribution inside BiVO<sub>4</sub> homojunction, selective deposition of Ag<sub>2</sub>O onto BiVO<sub>4</sub> (110) crystal face and introduction of moderate RGO (1 wt. %, 3 wt. % and 5 wt. %) into BiVO<sub>4</sub> (040)/Ag<sub>2</sub>O composites have carried out, and the TEM images of products are displayed in Fig. S9. Considering that the work function of BiVO<sub>4</sub> (110) facet (5.51 eV) is larger than that of Ag<sub>2</sub>O crystal (4.8–5.1 eV), electrons will flow from Ag<sub>2</sub>O to BiVO<sub>4</sub> (110) facet until their Fermi levels are aligned at the same electric potential. In this process, the band near the BiVO<sub>4</sub> (110) facet are bent downward while the band near the Ag<sub>2</sub>O are bent upward in BiVO<sub>4</sub> (110)/Ag<sub>2</sub>O-3 composites (Fig. 7a). Under the circumstance, an insurmountable potential barrier has been generated and goes against the transmission of charge carriers between Ag<sub>2</sub>O and BiVO<sub>4</sub> (110) facet, ultimately restrains the charge density redistribution inside BiVO<sub>4</sub> homojunction [68,69]. As displayed in Fig. 7b and c, the photocatalytic degradation efficiency and O<sub>2</sub> generation ability of BiVO<sub>4</sub> (110)/Ag<sub>2</sub>O-3 composite (orange points) have been inhibited extremely compared with that of BA3 heterostructure (blue points) under various light irradiation, demonstrating the charge carrier transfer between Ag<sub>2</sub>O and BiVO<sub>4</sub> plays an important part in photocatalytic performances. Meanwhile, the dramatic deterioration of the photocatalytic capacity has been observed in all RGO/BiVO<sub>4</sub> (040)/Ag<sub>2</sub>O-3 serial composites, and the degradation rate reduces obviously with the increase of graphene content (Fig. 7e). According to this, inferred schematic diagram has been put forward to reveal the variation of charge carriers transport processes after the introduction of RGO into BA3 composite. As displayed in Fig. 7g, besides the intrinsic migration occurs along the interfaces of BiVO<sub>4</sub> (110) facet–BiVO<sub>4</sub> (040) facet–Ag<sub>2</sub>O (Case I in Fig. 7g), plenty of photo-induced electrons escape to the RGO surface (Case II in Fig. 7g) owing to the excellent conductivity of RGO. In this case, compared to BA3 composite, limited alteration of the relative Fermi level positions between (040) facet and (110) facet could be generated in RGO/BiVO<sub>4</sub> (040)/Ag<sub>2</sub>O-3 composites (Fig. 7g–α), accompanied by the inhibited interfacial band bending degree (Fig. 7g–β) inside BiVO<sub>4</sub> homojunction, which restrains the charge density redistribution and passivates the photocatalytic oxidation activity ultimately. Consequently, these inferior photocatalytic performances both illustrate that the charge density redistribution inside BiVO<sub>4</sub> homojunction plays a critical role in achieving the elevated photocatalytic oxidation capacities, and the selective deposition of

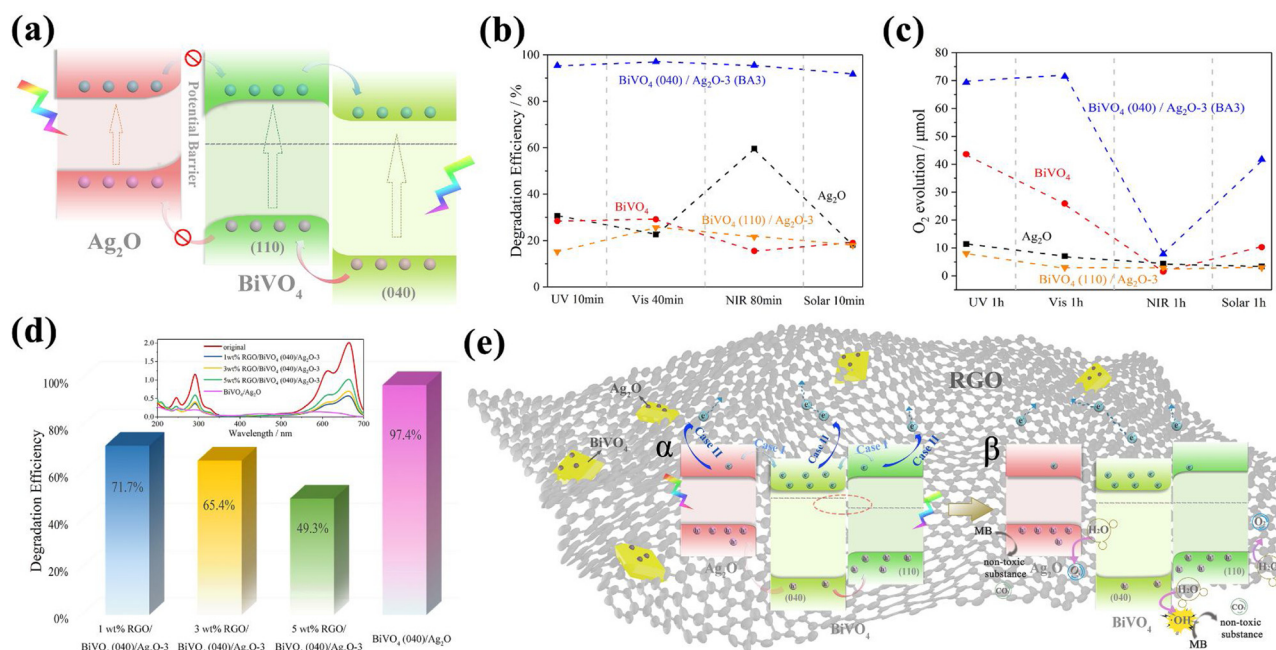


**Fig. 7.** Schematic diagram of the charge carrier separation and transport processes in (a) BiVO<sub>4</sub> (110)/Ag<sub>2</sub>O-3 composites and (e) RGO/BiVO<sub>4</sub> (040)/Ag<sub>2</sub>O-3 composites under UV or Vis light irradiation. (b) Photocatalytic degradation efficiency and (c) photocatalytic O<sub>2</sub> evolution over different samples under UV, Vis, NIR and solar light irradiation. (d) Photocatalytic degradation efficiency over different RGO/BiVO<sub>4</sub> (040)/Ag<sub>2</sub>O-3 samples after UV light irradiation for 10 min. The inset shows the absorption spectra of MB solution after 10 min photodegradation.

Ag<sub>2</sub>O onto BiVO<sub>4</sub> (040) facet is truly a rational pathway to regulate the photogenerated carrier separation and transfer.

### 3. Conclusion

In summary, a novel and efficient strategy to settle the high charge recombination probability in BiVO<sub>4</sub> homojunction has been realized via the selective deposition of Ag<sub>2</sub>O onto the high-active (040) facet of BiVO<sub>4</sub>. The as-prepared BiVO<sub>4</sub> (040)/Ag<sub>2</sub>O heterostructure exhibits a full-spectrum-responsive photocatalytic activity for highly efficient pollutant degradation and O<sub>2</sub> evolution, which could be attributed to the favorable synergistic effect of the crystal-face engineering of BiVO<sub>4</sub> and selective facet modification with Ag<sub>2</sub>O. In this hybridization system, Ag<sub>2</sub>O can serve on the light-harvesting agent as well as a mediator in refactoring the energy band structure of BiVO<sub>4</sub> homojunction to accelerate inside charge transfer. By this means, the BA3 composite exhibits a 15-fold enhancement on photooxidation of MB solution and 4-fold improvement on photocatalytic O<sub>2</sub> evolution as compared to the pure BiVO<sub>4</sub>, even though the bare Ag<sub>2</sub>O component is inert under the AM1.5 simulated solar light irradiation. Beyond the enhanced photocatalytic oxidation capacities and stabilities, this work also presents a rational strategy to design highly efficient photocatalysts to explore full advantages of solar energy in the future.

### Acknowledgments

This work is supported by the National Natural Science Funds of China (Nos. 51672115 and 21501080) and the Gansu Province Development and Reform Commission (NDRC, No. 2013-1336).

### Appendix A. Supplementary data

Supplementary material related to this article can be found, in the online version, at doi:<https://doi.org/10.1016/j.apcatb.2019.03.062>.

### References

- [1] H. Li, Y. Sun, B. Cai, S. Gan, D. Han, L. Niu, T. Wu, *Appl. Catal. B: Environ.* 170–171 (2015) 206–214.
- [2] X. Xu, F. Luo, W. Tang, J. Hu, H. Zeng, Y. Zhou, *Adv. Funct. Mater.* (2018) 1804055.
- [3] L. Bai, X. Wang, S. Tang, Y. Kang, J. Wang, Y. Yu, Z.K. Zhou, C. Ma, X. Zhang, J. Jiang, P.K. Chu, X.F. Yu, *Adv. Mater.* (2018) e1803641.
- [4] W. Zhao, Y. Liu, Z. Wei, S. Yang, H. He, C. Sun, *Appl. Catal. B: Environ.* 185 (2016) 242–252.
- [5] L. Zhang, W. Feng, B. Wang, K. Wang, F. Gao, Y. Zhao, P. Liu, *Appl. Catal. B: Environ.* 212 (2017) 80–88.
- [6] R. Li, H. Han, F. Zhang, D. Wang, C. Li, *Energ. Environ. Sci.* 7 (2014) 1369–1376.
- [7] T. Tachikawa, T. Ochi, Y. Kobori, *ACS Catal.* 6 (2016) 2250–2256.
- [8] J. Zhu, F. Fan, R. Chen, H. An, Z. Feng, C. Li, *Angew. Chem. Int. Ed.* 54 (2015) 9111–9114.
- [9] T. Wang, C. Li, J. Ji, Y. Wei, P. Zhang, S. Wang, X. Fan, J. Gong, *ACS Sustain. Chem. Eng.* 2 (2014) 2253–2258.
- [10] T.W. Kim, K.-S. Choi, *Science* (2014).
- [11] J. Pan, G. Liu, G.Q. Lu, H.M. Cheng, *Angew. Chem. Int. Ed.* 50 (2011) 2133–2137.
- [12] P. Li, Y. Zhou, Z. Zhao, Q. Xu, X. Wang, M. Xiao, Z. Zou, *J. Am. Chem. Soc.* 137 (2015) 9547–9550.
- [13] C.W. Kim, Y.S. Son, M.J. Kang, D.Y. Kim, Y.S. Kang, *Adv. Energy Mater.* 6 (2016) 1501754.
- [14] L. Zhang, W. Wang, S. Sun, D. Jiang, E. Gao, *Appl. Catal. B: Environ.* 162 (2015) 470–474.
- [15] R. Li, F. Zhang, D. Wang, J. Yang, M. Li, J. Zhu, X. Zhou, H. Han, C. Li, *Nat. Commun.* 4 (2013) 1432.
- [16] F. Lin, D. Wang, Z. Jiang, Y. Ma, J. Li, R. Li, C. Li, *Energy Environ. Sci.* 5 (2012) 6400–6406.
- [17] H.L. Tan, R. Amal, Y.H. Ng, *J. Mater. Chem. A* 5 (2017) 16498–16521.
- [18] M. Ou, S. Wan, Q. Zhong, S. Zhang, Y. Song, L. Guo, W. Cai, Y. Xu, *Appl. Catal. B: Environ.* 221 (2018) 97–107.
- [19] F. Chen, Q. Yang, X. Li, G. Zeng, D. Wang, C. Niu, J. Zhao, H. An, T. Xie, Y. Deng, *Appl. Catal. B: Environ.* 200 (2017) 330–342.
- [20] W. Songcan, C. Peng, Y. Jung-Ho, H. Yuxiang, W. Lianzhou, *Angew. Chem. Int. Ed.* 56 (2017) 8500–8504.
- [21] H. Li, H. Yu, X. Quan, S. Chen, H. Zhao, *Adv. Funct. Mater.* 25 (2015) 3074–3080.
- [22] J. Tian, Y. Leng, Z. Zhao, Y. Xia, Y. Sang, P. Hao, J. Zhan, M. Li, H. Liu, *Nano Energy* 11 (2015) 419–427.
- [23] X. Chen, L. Liu, F. Huang, *Chem. Soc. Rev.* 44 (2015) 1861–1885.
- [24] X. Liu, W. Di, W. Qin, *Appl. Catal. B: Environ.* 205 (2017) 158–164.
- [25] S. Huang, N. Zhu, Z. Lou, L. Gu, C. Miao, H. Yuan, A. Shan, *Nanoscale* 6 (2014) 1362–1368.
- [26] Y. Chen, G. Zhu, M. Hojamberdiev, J. Gao, R. Zhu, C. Wang, X. Wei, P. Liu, *J. Hazard. Mater.* 344 (2018) 42–54.
- [27] J. Chen, H. Che, K. Huang, C. Liu, W. Shi, *Appl. Catal. B: Environ.* 192 (2016) 134–144.
- [28] C. Yu, G. Li, S. Kumar, K. Yang, R. Jin, *Adv. Mater.* 26 (2014) 892–898.



- [29] N. Wei, H. Cui, Q. Song, L. Zhang, X. Song, K. Wang, Y. Zhang, J. Li, J. Wen, J. Tian, *Appl. Catal. B: Environ.* 198 (2016) 83–90.
- [30] N. Liang, M. Wang, L. Jin, S. Huang, W. Chen, M. Xu, Q. He, J. Zai, N. Fang, X. Qian, *ACS Appl. Mater. Inter.* 6 (2014) 11698–11705.
- [31] C. Li, P. Zhang, R. Lv, J. Lu, T. Wang, S. Wang, H. Wang, J. Gong, *Small* 9 (2013) 3951–3956, 3950.
- [32] H.J. Kong, D.H. Won, J. Kim, S.I. Woo, *Chem. Mater.* 28 (2016) 1318–1324.
- [33] J. Yu, A. Kudo, *Adv. Funct. Mater.* 16 (2006) 2163–2169.
- [34] S. Gu, W. Li, F. Wang, S. Wang, H. Zhou, H. Li, *Appl. Catal. B: Environ.* 170–171 (2015) 186–194.
- [35] T. Liu, B. Liu, L. Yang, X. Ma, H. Li, S. Yin, T. Sato, T. Sekino, Y. Wang, *Appl. Catal. B: Environ.* 204 (2017) 593–601.
- [36] L. Tang, C. Feng, Y. Deng, G. Zeng, J. Wang, Y. Liu, H. Feng, J. Wang, *Appl. Catal. B: Environ.* 230 (2018) 102–114.
- [37] H. Yang, J. Tian, T. Li, H. Cui, *Catal. Commun.* 87 (2016) 82–85.
- [38] S.M. Thalluri, S. Hernández, S. Bensaid, G. Saracco, N. Russo, *Appl. Catal. B: Environ.* 180 (2016) 630–636.
- [39] S.-F. Yang, C.-G. Niu, D.-W. Huang, H. Zhang, C. Liang, G.-M. Zeng, *Environ. Sci. Nano* 4 (2017) 585–595.
- [40] S. Gao, C. Guo, J. Lv, Q. Wang, Y. Zhang, S. Hou, J. Gao, J. Xu, *Chem. Eng. J.* 307 (2017) 1055–1065.
- [41] C. Wang, L. Zhu, C. Song, G. Shan, P. Chen, *Appl. Catal. B: Environ.* 105 (2011) 229–236.
- [42] H. Xu, J. Xie, W. Jia, G. Wu, Y. Cao, J. Colloid Interf. Sci. 516 (2018) 511–521.
- [43] Y. Li, Q. Wang, H. Wang, J. Tian, H. Cui, J. Colloid Interf. Sci. 537 (2019) 206–214.
- [44] X. Wang, S. Li, H. Yu, J. Yu, S. Liu, *Chem. Eur. J.* 17 (2011) 7777–7780.
- [45] Y. Li, S. Ouyang, H. Xu, X. Wang, Y. Bi, Y. Zhang, J. Ye, *J. Am. Chem. Soc.* (2016).
- [46] Q. Han, B. Wang, J. Gao, Z. Cheng, Y. Zhao, Z. Zhang, L. Qu, *ACS Nano* 10 (2016) 2745–2751.
- [47] C. Zhou, C. Lai, D. Huang, G. Zeng, C. Zhang, M. Cheng, L. Hu, J. Wan, W. Xiong, M. Wen, X. Wen, L. Qin, *Appl. Catal. B: Environ.* 220 (2018) 202–210.
- [48] B. Xu, Y. An, Y. Liu, X. Qin, X. Zhang, Y. Dai, Z. Wang, P. Wang, M.-H. Whangbo, B. Huang, *J. Mater. Chem. A* 5 (2017) 14406–14414.
- [49] L. Pan, S. Wang, J. Xie, L. Wang, X. Zhang, J.-J. Zou, *Nano Energy* 28 (2016) 296–303.
- [50] X. Men, H. Chen, K. Chang, X. Fang, C. Wu, W. Qin, S. Yin, *Appl. Catal. B: Environ.* 187 (2016) 367–374.
- [51] H. Huang, S. Tu, C. Zeng, T. Zhang, A.H. Reshak, Y. Zhang, *Angew. Chem. Int. Ed. Engl.* 56 (2017) 11860–11864.
- [52] Y.S. Wang, J.H. Shen, J.J. Horng, *J. Hazard. Mater.* 274 (2014) 420–427.
- [53] M. Chen, Y. Huang, S.C. Lee, *Chinese J. Catal.* 38 (2017) 348–356.
- [54] J. Hu, D. Chen, Z. Mo, N. Li, Q. Xu, H. Li, J. He, H. Xu, J. Lu, *Angew. Chem. Int. Ed.* 58 (2019) 2073–2077.
- [55] Z. Cheng, T.A. Shifa, F. Wang, Y. Gao, P. He, K. Zhang, C. Jiang, Q. Liu, J. He, *Adv. Mater.* 30 (2018) e1707433.
- [56] X. Wu, J. Zhao, L. Wang, M. Han, M. Zhang, H. Wang, H. Huang, Y. Liu, Z. Kang, *Appl. Catal. B: Environ.* 206 (2017) 501–509.
- [57] J. Liu, Y. Liu, N. Liu, Y. Han, X. Zhang, H. Huang, Y. Lifshitz, S.-T. Lee, J. Zhong, Z. Kang, *Science* 347 (2015) 970–974.
- [58] B. Tian, Q. Lei, B. Tian, W. Zhang, Y. Cui, Y. Tian, *Chem. Commun.* 54 (2018) 1845–1848.
- [59] C. Zhou, S. Wang, Z. Zhao, Z. Shi, S. Yan, Z. Zou, *Adv. Funct. Mater.* 28 (2018) 1801214.
- [60] M.A. Muhsien, H.H. Hamdan, *Energy Procedia* 18 (2012) 300–311.
- [61] Z. Zhang, J.T. Yates Jr., *Chem. Rev.* 112 (2012) 5520–5551.
- [62] J. Low, J. Yu, M. Jaroniec, S. Wageh, A.A. Al-Ghamdi, *Adv. Mater.* 29 (2017).
- [63] J. Low, B. Dai, T. Tong, C. Jiang, J. Yu, *Adv. Mater.* (2018) e1802981.
- [64] Z. Jiang, W. Wan, H. Li, S. Yuan, H. Zhao, P.K. Wong, *Adv. Mater.* 30 (2018).
- [65] J.W. Ha, T.P. Ruberu, R. Han, B. Dong, J. Vela, N. Fang, *J. Am. Chem. Soc.* 136 (2014) 1398–1408.
- [66] J. Yan, T. Wang, G. Wu, W. Dai, N. Guan, L. Li, J. Gong, *Adv. Mater.* 27 (2015) 1580–1586.
- [67] C. Hao, W. Wang, R. Zhang, B. Zou, H. Shi, *Sol. Energy Mater. Sol. C* 174 (2018) 132–139.
- [68] L.J. Zhang, S. Li, B.K. Liu, D.J. Wang, T.F. Xie, *ACS Catal.* 4 (2014) 3724–3729.
- [69] J. Hu, L. Wang, P. Zhang, C. Liang, G. Shao, *J. Power Sources* 328 (2016) 28–36.